

## PROTOSTAR FORMATION IN SUPERSONIC FLOWS: GROWTH AND COLLAPSE OF SPHERICAL CORES

HAO GONG AND EVE C. OSTRIKER

Department of Astronomy, University of Maryland, College Park, MD 20742-2421, USA; hgong@astro.umd.edu, ostriker@astro.umd.edu  
Received 2009 February 18; accepted 2009 April 24; published 2009 June 10

### ABSTRACT

We present a unified model for molecular core formation and evolution, based on numerical simulations of converging, supersonic flows. Our model applies to star formation in giant molecular clouds dominated by large-scale turbulence, and contains four main stages: core building, core collapse, envelope infall, and late accretion. During the building stage, cores form out of dense, post-shock gas, and become increasingly centrally stratified as the mass grows over time. Even for highly supersonic converging flows, the dense gas is subsonic, consistent with observations showing quiescent cores. When the shock radius defining the core boundary exceeds  $R \approx 4a(4\pi G\rho_{\text{mean}})^{-1/2}$ , where  $a$  is the isothermal sound speed, a wave of collapse propagates from the edge to the center. During the building and collapse stages, density profiles can be fitted by Bonnor–Ebert profiles with temperature 1.2–2.9 times the true value, similar to many observed cores. As found previously for initially static equilibria, outside-in collapse leads to a Larson–Penston density profile  $\rho \approx 8.86a^2/(4\pi Gr^2)$ . The third stage, consisting of an inside-out wave of gravitational rarefaction leading to  $\rho \propto r^{-3/2}$ ,  $v \propto r^{-1/2}$ , is also similar to that for initially static spheres, as originally described by Shu. We find that the collapse and infall stages have comparable duration,  $\sim t_{\text{ff}}$ , consistent with estimates for observed prestellar and protostellar (Class 0/I) cores. Core building takes longer, but does not produce high-contrast objects until shortly before collapse. The time to reach core collapse, and the core mass at collapse, decrease with increasing inflow Mach number. For all cases, the accretion rate is  $\gg a^3/G$  early on but sharply drops off; the final system mass depends on the duration of late-stage accretion, set by large-scale conditions in a cloud.

*Key words:* ISM: clouds – ISM: globules – stars: formation

### 1. INTRODUCTION

Dense molecular cores are the immediate precursors of new stars on small scales, and understanding how they grow and evolve is fundamental to the theory of star formation (Shu et al. 1987; McKee & Ostriker 2007). Because many elements are involved in core formation, complete theoretical models have not yet been developed, and it is not yet clear whether a single dynamical effect dominates the overall process, or whether several contributing effects have comparable importance. In one limit that has been studied in some detail, ambient velocities are negligible, and self-gravitating cores form by the slow diffusion of partially ionized gas through strongly supporting magnetic fields until a supercritical configuration is reached (e.g., Mouschovias & Ciolek 1999). In another limit, which has been considered more recently—but in much less detail at core scales, magnetic support is negligible, and supersonic turbulence creates and destroys condensations, with some fraction of this gas sufficiently dense and long-lived that it can undergo collapse (e.g., Mac Low & Klessen 2004). As observed clouds are both magnetized and strongly turbulent, the eventual theory for core formation that is developed must account for both processes; pioneering work toward this goal has begun (e.g., Kudoh & Basu 2008; Nakamura & Li 2008). Because of the technical challenges involved in building comprehensive models and the need to elucidate the contributing physics, it is important to develop simplified models in greater detail. In this contribution, we consider aspects of core growth and evolution in the turbulence-dominated, unmagnetized limit.

Increasingly detailed observations in recent years provide constraints on theoretical models (see, e.g., the reviews of Di Francesco et al. 2007; Ward-Thompson et al. 2007; André et al. 2008). One class of observations focuses on the density distribution within cores. One-dimensional (angle-averaged)

density profiles (e.g., Ward-Thompson et al. 1994; Shirley et al. 2000; Bacmann et al. 2000; Evans et al. 2001; Alves et al. 2001; Kirk et al. 2005; Kandori et al. 2005) generally show a uniform-density center surrounded by a power-law envelope extending to an outer radius  $\sim 0.1$  pc, which is consistent with the density profile of a static, isothermal, unmagnetized Bonnor–Ebert (hereafter BE) sphere (Bonnor 1956; Ebert 1955). The interpretation in terms of static equilibrium is problematic, however, insofar as many cases show center-to-edge density contrasts exceeding the maximum ratio ( $\rho_c/\rho_{\text{edge}} = 14.0$ ; here  $\rho_c$  is the central density) that would be stable against collapse, and would also require central temperatures greater than observed values in order to provide support for the total masses inferred from the integrated continuum emission. In addition, cores are generally not isolated; rather than being surrounded by a high-temperature, low-density medium with pressure matching the core’s outer edge, they are surrounded by moderate-density cold molecular gas representing clumps and filaments within larger clouds (Bergin & Tafalla 2007). The interpretation of observed density profiles as static solutions is also not unique, in that dynamically collapsing cores initiated from near-critical equilibrium show the same density profiles as (supercritical) static solutions (see, e.g., Myers 2005; Kandori et al. 2005, and below). Concentrations formed within turbulent flows can also have density profiles resembling BE spheres (Ballesteros-Paredes et al. 2003).

Velocity information can distinguish between static, oscillating (Keto et al. 2006; Broderick et al. 2007), and collapsing cores, and can potentially also help discriminate how these cores formed out of more diffuse gas. Dense, low-mass cores generally have subsonic internal velocity dispersions, whether for isolated cores or for cores found in clusters (e.g., Myers 1983; Goodman et al. 1998; Caselli et al. 2002; Kirk et al. 2007; André et al. 2007; Lada et al. 2008). In cores containing protostars,

signatures of infall on small scales ( $\sim 0.01\text{--}0.1$  pc), believed to be indicative of gravitational collapse, have been observed via the asymmetry of molecular lines that trace high-density gas (e.g., Zhou et al. 1993; Mardones et al. 1997; Gregersen et al. 1997; Di Francesco et al. 2001). For prestellar cores, inward motions are often evident over both small ( $\lesssim 0.1$  pc) and larger scales ( $\sim 0.1\text{--}0.4$  pc), sometimes encompassing a whole star-forming complex (Lee et al. 1999, 2001; Walsh et al. 2006; see also Peretto et al. 2006). Small-scale inward motions within cores are subsonic (Lee et al. 2001), while larger-scale motions can be transonic or supersonic (Walsh et al. 2006 infer higher velocities in lower-density gas), and may be indicative of converging larger-scale flows in which dense gas builds up in a shock-bound stagnation region.

The relative durations of prestellar and protostellar (i.e., containing an accreting embedded Class 0 or I object) stages of core evolution are determined by comparing the relative numbers of the two classes of sources in a given cloud. Absolute core lifetimes are further obtained by comparison to the number of T Tauri stars with measured ages. Several studies using this statistical approach in different clouds have reached similar conclusions: the durations of the prestellar and accreting stages of cores are comparable (Beichman et al. 1986; Lee & Myers 1999; Jessop & Ward-Thompson 2000; Kirk et al. 2005; Jørgensen et al. 2007; Hatchell et al. 2007; Enoch et al. 2008; Evans et al. 2009). Typical prestellar core lifetimes are estimated at  $\sim 2\text{--}5 \times 10^5$  yr, amounting to a few times the free-fall time

$$t_{\text{ff}} \equiv \left( \frac{3\pi}{32G\bar{\rho}} \right)^{1/2} = 1.37 \times 10^5 \text{ yr} \left( \frac{\bar{n}_H}{10^5 \text{ cm}^{-3}} \right)^{-1/2} \quad (1)$$

measured at the mean core density  $\bar{\rho} = 1.4m_H\bar{n}_H$ . With lifetimes considerably below the ambipolar diffusion time for strong magnetic fields  $t_{\text{AD}} \approx 10t_{\text{ff}}$  (e.g., Mouschovias & Ciolek 1999), this suggests that observed cores are gravitationally supercritical with respect to the magnetic field. This conclusion is also supported by magnetic field Zeeman observations, indicating that cores have mean mass-to-magnetic flux ratios two times the critical value (Troland & Crutcher 2008). Since cores are only identified in millimeter and submillimeter continuum when the  $n_H$  exceeds a few  $\times 10^4 \text{ cm}^{-3}$ , in principle it is possible that an extended period of slow diffusion at lower density precedes the observed core stage. Turbulence accelerates ambipolar diffusion, however (e.g., Zweibel 2002; Fatuzzo & Adams 2002; Li & Nakamura 2004; Heitsch et al. 2004), so it is also possible that the flux loss needed to reach a magnetically supercritical state may occur more dynamically, at densities below  $10^4 \text{ cm}^{-3}$ .

Theoretical modeling of core evolution has a long history. Much work has focused on the evolution of unstable thermally supported equilibria into collapse (formally resulting in infinite density at the origin), followed by accretion of the envelope. Self-similar solutions for collapse and/or accretion stages of isothermal spheres were found by Larson (1969), Penston (1969), Shu (1977), and Hunter (1977); these were later generalized by Whitworth & Summers (1985). Larson (1969) and Penston (1969) (hereafter LP) independently found self-similar solutions which describe the density and velocity prior to the instant of protostar formation (defined as the instant at which the central density becomes infinite). In the LP solution, the radial velocity approaches a constant value  $-3.28a$  and the density approaches

$$\rho = 8.86 \frac{a^2}{4\pi Gr^2} \quad (2)$$

at the instant of central protostar formation, with mass inflow rate  $\dot{M} = 29.1 a^3/G$ . Here,  $a$  is the isothermal sound speed, and the dimensional factor in the accretion rate is given by

$$\frac{a^3}{G} = 1.6 \times 10^{-6} M_{\odot} \text{ yr}^{-1} \left( \frac{T}{10 \text{ K}} \right)^{3/2}. \quad (3)$$

The analysis of Shu (1977) showed that for an initial profile that is a static singular isothermal sphere,  $\rho = 2a^2/(4\pi Gr^2)$ , evolution yields an “inside-out” infall solution in which a wave of rarefaction propagates outward at the sound speed. Inside of the expansion wave, the mass inflow rate is  $\dot{M} = 0.975 a^3/G$  independent of  $r$ , and gas accelerates to free fall ( $v \propto r^{-1/2}$ ,  $\rho \propto r^{-3/2}$ ). Hunter (1977) connected and extended the investigations of LP (which address evolution prior to protostar formation) with that of Shu (which focuses on the accretion stage). He showed that self-similar solutions before and after the point of singularity formation (i.e.,  $t = 0$ ) can be smoothly matched. This allowed the LP solution to be extended into the accretion phase with similar free-fall behavior near the origin; Hunter (1977) also found a sequence of self-similar solutions valid for all time that approach the Shu (1977) expansion wave solution.

Many numerical simulations of isothermal collapse have shown that the density in the core approaches a  $\rho \propto r^{-2}$  profile at the point of protostar formation, regardless of how collapse is initiated (Bodenheimer & Sweigart 1968; Larson 1969; Penston 1969; Hunter 1977; Foster & Chevalier 1993; Ogino et al. 1999; Hennebelle et al. 2003; Motoyama & Yoshida 2003; Vorobyov & Basu 2005; Gómez et al. 2007). These simulations include initiation from a static configuration that is unstable, and initiation from static, stable configurations that are subjected to transient compression, either from enhanced external pressure or a converging velocity field. Another feature common to the results from simulations is that the collapse generally begins on the outside, with the infalling region propagating inward as the central density increases. At the time of singularity formation, the central velocity has been found to be comparable to the value  $-3.3a$  derived by LP, with the density normalization also similar to the LP result (Foster & Chevalier 1993; Ogino et al. 1999). Following the instant of protostar formation, the evolution of the mass accretion rate over time depends strongly on the initial conditions, however.

Simulations with triggered core collapse (Hennebelle et al. 2003; Motoyama & Yoshida 2003) are motivated by the fact that star-forming regions are highly dynamic, such that external compression may significantly affect core internal evolution, and enhance the accretion rate by raising the central density. Triggering events may be associated with high-mass star formation, but even without these highly energetic events, the large-scale turbulence that pervades giant molecular clouds (GMCs) can compress initially quiescent cores. Taking this idea one step further, it is interesting to consider not just the core-collapse process, but also the core formation process, in a strongly turbulent medium. Gómez et al. (2007) conducted one such study, considering how an impulsive converging velocity field can create gravitationally bound, centrally concentrated cores. Core formation induced by supersonic turbulence has also been studied in a number of numerical simulations that focus on the large scales, with much of the emphasis on determining the distribution of core masses for comparison to observed core mass functions and the stellar initial mass function (IMF; see, e.g., the review of McKee & Ostriker 2007). However, these studies have not had sufficient resolution to investigate the internal properties of the cores that form. If the mass of a core is built up over time

as the post-shock product of colliding supersonic flows, what is the detailed evolution leading up to collapse, and during the accretion phase?

In this paper, we initiate a study of dynamically induced core formation and collapse by considering perhaps the simplest possible situation: a supersonic, converging, spherical flow. Our initial conditions are a uniform low-density medium with no stratification. A dense core forms inside a spherical shock, and over time becomes stratified as its mass grows and it becomes self-gravitating. When the stratification becomes too great, collapse and subsequent accretion occurs in a similar manner to the case of an initially unstable static equilibrium. We consider cases of varying inflow Mach number, and with the large-scale inflow either steady over all time, or shut off after an interval.

The condition of spherical inflow that we adopt for this first study is, of course, likely to be rare in real clouds. As the main purpose of this study is to take the first step toward unified models of core formation and collapse in dynamic environments, however, we consider one-dimensional solutions the natural place to start. We shall show that many features consistent with observed cores are evident even in these idealized models, suggesting that they are generic to dynamic core formation scenarios. The present set of simulations, in addition to enabling identification of characteristic evolutionary stages, also serve as a useful reference point for more realistic but more complex simulations. More typical than a converging spherical flow would be a converging planar flow, which yields a dense post-shock stagnation layer in which self-gravitating cores can form. Numerical studies that we have begun for supersonic planar inflows show results for core building and collapse that are qualitatively similar to the present results for supersonic spherical inflows.

The plan of this paper is as follows: in Section 2, we present the governing equations and describe our problem specification and numerical method. Section 3 briefly describes results of collapse initiated from static configurations, demonstrating that we reproduce prior results, and providing a baseline for comparison to our models of dynamic formation and collapse. Section 4 presents numerical results for our converging-flow simulations, covering the stage of core formation and evolution up to the point of singularity formation in Section 4.1 and the subsequent stages in Section 4.2. We introduce a breakdown into new physically defined stages in Section 4.3, and quantify the evolution of accretion rates in Section 4.4. Section 5 summarizes our new results and discusses our findings in the context of previous theory and observations.

## 2. GOVERNING EQUATIONS AND NUMERICAL METHODS

The equations of motion for a spherically symmetric flow take the form:

$$\frac{\partial \rho}{\partial t} + \frac{1}{r^2} \frac{\partial (r^2 \rho v)}{\partial r} = 0, \quad (4)$$

$$\frac{\partial v}{\partial t} + v \frac{\partial v}{\partial r} = -\frac{1}{\rho} \frac{\partial P}{\partial r} - \frac{GM(r)}{r^2}, \quad (5)$$

where  $M$  is the mass within radius  $r$  defined by  $dM = 4\pi r^2 \rho dr$ ,  $v$  is the radial velocity,  $P$  is the gas pressure, and  $\rho$  is the density. For prestellar collapse, an isothermal equation of state  $P = a^2 \rho$  is often used, because cooling is so efficient that the gas remains at nearly constant temperature during the

gravitational collapse (Larson 1969; Nakamura 1998). We adopt an isothermal equation of state.

For ease of comparison with previous work, we introduce the following dimensionless variables:

$$\tau \equiv t/t_0, \quad (6)$$

$$\xi \equiv r/r_0, \quad (7)$$

$$D \equiv \rho/\rho_0, \quad (8)$$

$$u \equiv v/a, \quad (9)$$

$$m \equiv M/M_0. \quad (10)$$

Here,  $\rho_0$  is a fiducial density representing the volume-averaged ambient density in a cloud on large scales, which we shall later set to the uniform density of the converging flow. The unit of velocity is the isothermal sound speed

$$a = 0.19 \text{ km s}^{-1} \left( \frac{T}{10 \text{ K}} \right)^{1/2}, \quad (11)$$

the unit of time is related to the free-fall time at the fiducial density by

$$t_0 \equiv \frac{1}{(4\pi G \rho_0)^{1/2}} = 0.52 t_{\text{ff}} = 2.3 \times 10^6 \text{ yr} \left( \frac{n_H}{10^2 \text{ cm}^{-3}} \right)^{-1/2}, \quad (12)$$

the unit of length is related to the Jeans length at the fiducial density  $L_J \equiv a(\pi/G\rho_0)^{1/2}$  by

$$\begin{aligned} r_0 &\equiv \frac{a}{(4\pi G \rho_0)^{1/2}} = \frac{L_J}{2\pi} \\ &= 0.44 \text{ pc} \left( \frac{T}{10 \text{ K}} \right)^{1/2} \left( \frac{n_H}{10^2 \text{ cm}^{-3}} \right)^{-1/2}, \end{aligned} \quad (13)$$

and the corresponding basic unit of mass is  $\rho_0 r_0^3 = a^3/[4\pi(4\pi G^3 \rho_0)^{1/2}]$ . The mass unit adopted in Equation (10) is larger than this by a factor  $4\pi$ :

$$M_0 \equiv \frac{a^3}{(4\pi G^3 \rho_0)^{1/2}} = 3.7 M_\odot \left( \frac{T}{10 \text{ K}} \right)^{3/2} \left( \frac{n_H}{10^2 \text{ cm}^{-3}} \right)^{-1/2}. \quad (14)$$

With the dimensionless variables, the fluid equations become

$$\frac{\partial D}{\partial \tau} + \frac{1}{\xi^2} \frac{\partial (\xi^2 D u)}{\partial \xi} = 0, \quad (15)$$

$$\frac{\partial u}{\partial \tau} + u \frac{\partial u}{\partial \xi} = -\frac{1}{D} \frac{\partial D}{\partial \xi} - \frac{m}{\xi^2}, \quad (16)$$

$$m = \int D \xi^2 d\xi. \quad (17)$$

We solve the one-dimensional hydrodynamic Equations (15)–(17) with the ZEUS-2D (Stone & Norman 1992) code, in spherical symmetry. During the evolution to singularity formation (collapse phase), we adopt an inner reflecting boundary condition. For the post-collapse accretion phase, we implement a sink cell (Boss & Black 1982; Ogino et al. 1999) at the origin when the central density reaches a reference value. Subsequently, the inner boundary condition is changed to outflow, and the value of the central point mass is tracked via the integrated flow off the grid, with  $\dot{M}_{\text{ctr}} = (a^3/G) D_{\text{in}} u_{\text{in}} \xi_{\text{in}}^2$ . The sink cell is only implemented after the inflow in the central region becomes supersonic, so that information from the inner boundary cannot propagate into the remainder of the grid.



### 3. EVOLUTION OF INITIALLY STATIC CORES

As discussed in Section 1, many previous numerical simulations of core evolution have adopted static initial conditions and a fixed total mass (e.g., Hunter 1977; Foster & Chevalier 1993; Ogino et al. 1999; Vorobyov & Basu 2005). The adopted initial density profile shapes are consistent with (or similar to) a hydrostatic equilibrium, i.e., a BE sphere, with the initial density perturbed above the value that can be supported by the internal pressure in order to initiate collapse. These fixed-mass simulations adopt a prescribed external pressure at a low density with an effectively Lagrangian outer boundary (Hunter 1977), or else a fixed outer boundary with prescribed external pressure and no mass inflow (Ogino et al. 1999; Vorobyov & Basu 2005). Foster & Chevalier (1993) explored both types of boundary conditions, and found very similar results for a given initial cloud density profile. They concluded that the evolution for the fixed-mass case is insensitive to the outer boundary condition for initially unstable equilibria. This is consistent with the argument of Bodenheimer & Sweigart (1968) that the outer boundary condition does not affect evolution up to collapse as long as the free-fall time (Equation (1)) is shorter than the cloud crossing time. The ratio of the free-fall time at the mean density to the sound crossing time  $r_{\max}/a$  over the radius of a BE sphere is  $\pi/(8\xi \frac{d\Psi}{d\xi})^{1/2}$ , which approaches  $\pi/4 \sim 0.785$  as  $\xi$  approaches infinity. Here,  $\Psi = \Phi/a^2$ , the dimensionless gravitational potential. For the critical case, the free-fall time is 0.71 times the sound crossing time over the radius.

For comparison to previous work, we consider collapse of an initially static BE sphere. For initial conditions, we adopt a critical BE sphere, i.e., the outer boundary of the grid is at radius

$$\begin{aligned} R_{\text{BE,crit}} &= 6.45 \frac{a}{(4\pi G \rho_c)^{1/2}} = 1.72 \frac{a}{(4\pi G \rho_{\text{edge}})^{1/2}} \\ &= 2.70 \frac{a}{(4\pi G \rho_{\text{mean}})^{1/2}} \end{aligned} \quad (18)$$

corresponding to dimensionless outer radius  $\xi_e = \xi_{\text{crit}} = 6.45(\rho_0/\rho_c)^{1/2}$ . Here,  $\rho_{\text{mean}} = 2.45\rho_{\text{edge}}$  is the total core mass divided by its volume. The mass of the critical BE sphere is

$$\begin{aligned} M_{\text{BE,crit}} &= 1.18 \frac{a^4}{(G^3 P_{\text{edge}})^{1/2}} = 4.18 \frac{a^3}{(4\pi G^3 \rho_{\text{edge}})^{1/2}} \\ &= 1.5 M_{\odot} \left( \frac{T}{10 \text{ K}} \right)^{3/2} \left( \frac{n_{H,\text{edge}}}{10^4 \text{ cm}^{-3}} \right)^{-1/2}. \end{aligned} \quad (19)$$

To initiate collapse, density is perturbed above the equilibrium value by 10%. Our outer boundary condition is at a fixed pressure, with no inflow. The temporal evolution of the accretion rate for this model is shown in Figure 1.

Features similar to those outlined by Vorobyov & Basu (2005) are observed in our simulation. The accretion rate peaks at a value approaching the LP prediction at the instant when the central density (formally) becomes infinite, and steeply decreases thereafter. Vorobyov & Basu (2005) find that the decline in the accretion rate after singularity formation (unlike the increase in the accretion rate in Hunter's self-similar extension of the LP solution) can be attributed to the variation of velocity with radius in the sphere as it evolves toward collapse. We also considered cases of much larger initial static spheres, with outer boundaries  $\xi_e = 5 \xi_{\text{crit}}$  corresponding to highly unstable BE configurations. For these cases, the accretion rate decreases until it reaches a plateau at  $\dot{M} = 1.45 a^3/G$ ,

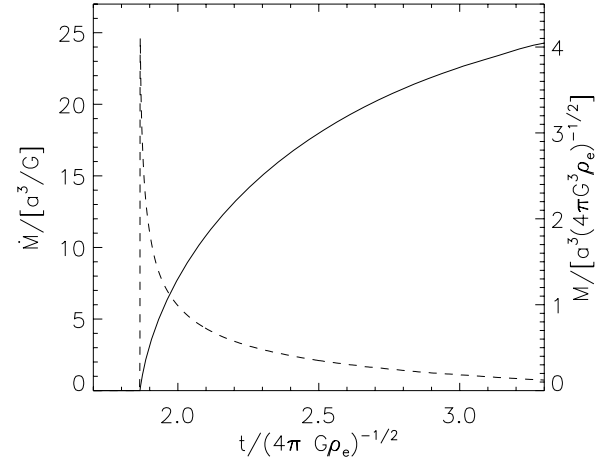


**Figure 1.** Dashed curve, left scale: the temporal evolution of the mass accretion rate at inner edge of the grid, for collapse initiated from a critical BE sphere (see Equation (3) for units). The solid curve, right scale: evolution of the central point mass (see Equation (14) for units). Time is shown in units scaled by the density at the outer edge (see Equation (12)).

consistent with the value reported in Shu (1977) (when the density is 10% greater than for hydrostatic equilibrium), and then further declines to zero after a rarefaction wave propagates inward from the outer boundary to reach the center.

Similar to the results of previous simulations, we find that the first collapse is “outside-in,” with velocities initially nonzero only in the outer parts where the imbalance between gravity and pressure is largest.<sup>1</sup> This is because the inner portions of the sphere, at  $\xi < \xi_{\text{crit}}$ , initially are equivalent to *stable* BE solutions. In all of our models initiated from static spheres, the density profile approaches the LP self-similar solution  $D = 8.86\xi^{-2}$ , and the velocity in the inner region approaches  $-3.28a$ , at the moment of singularity formation. Before this time, the density profile in the central region is flat with a magnitude that increases over time. The process can be thought of as a wave of compression propagating from the outside to the inside, creating a density distribution in which the ratio of radius to the Jeans length at the local density is everywhere constant:  $r/L_J(r) \approx \sqrt{8.86}/2\pi \approx 0.47$ . The singularity represents the instant the compression wave converges at the center.

Supersonic inflow velocities can be achieved without shock formation in the interior of the core (except at  $r = 0$ ) because inward acceleration occurs at all radii where the inward gravitational force exceeds the outward pressure force. By construction, the solutions initiated from static configurations all have gravity (slightly) exceeding pressure forces everywhere in the initial state, so that the inward acceleration is nonzero. After a singularity forms at the center, accretion begins, and the flow in the interior transitions from the  $v = \text{const.}, \rho \propto r^{-2}$  LP solution to a free-fall solution, with the accreting region propagating from the interior to the exterior in a manner similar to that described by Shu (1977). Thus, while collapse develops in an “outside-in” fashion, accretion develops in an “inside-out” fashion. Note that accretion in any centrally concentrated configuration should work its way outward from the center, because gravitational collapse times decline outward  $\propto \rho^{-1/2}$ , which is  $t_{\text{ff}} \propto r$  for an inverse-square density profile (true for either the LP profile or the singular isothermal sphere).

<sup>1</sup> For cases where the initial sphere is larger than the critical BE sphere, collapse begins at radii near  $\xi_{\text{crit}}$ , as was previously shown by Foster & Chevalier (1993).

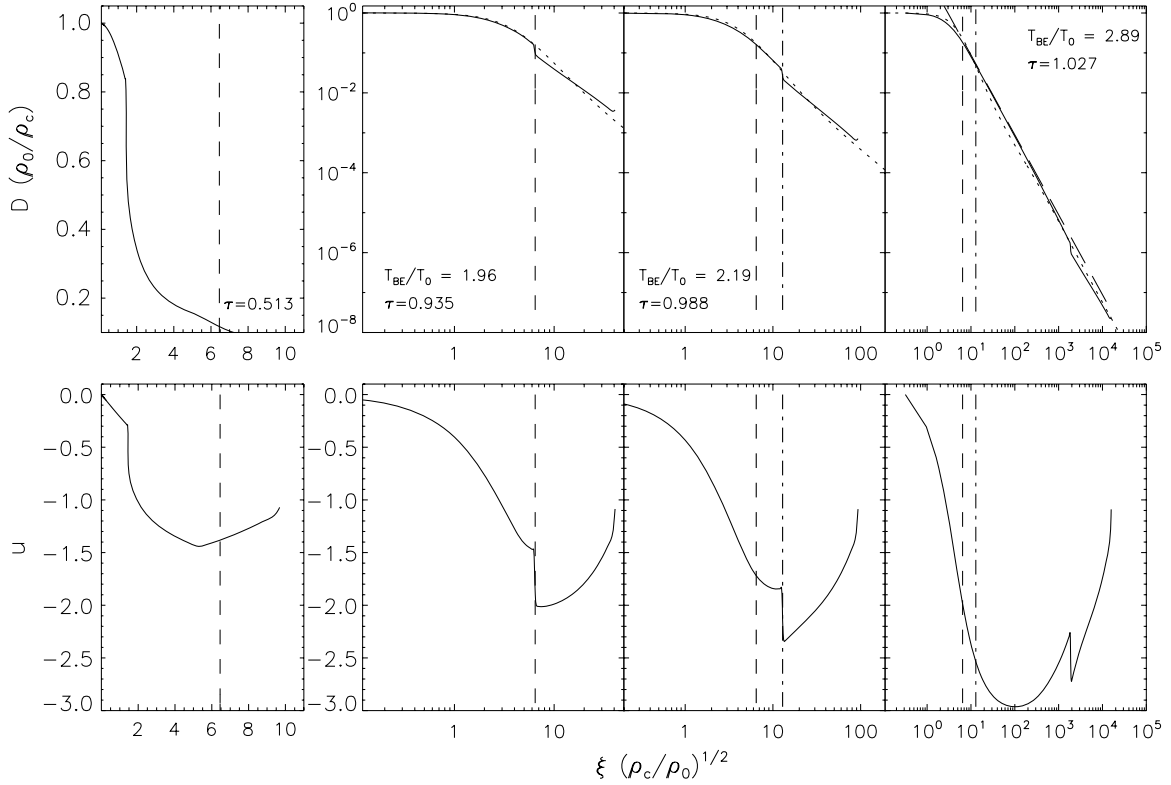


**Figure 2.** Density and velocity profiles (solid lines) for converging-flow model with  $M_a = 1.05$ , at times  $\tau$  as noted in the upper panel for each pair. The radius is normalized by the central density, i.e., the abscissa is  $r(4\pi G\rho_c)^{1/2}/a$ . For the three upper panels on the right, the dotted line is a fit to a BE sphere with temperature  $T_{BE}$ , with the fitted temperature noted in each panel. The dashed vertical lines denote the critical radius of a BE sphere with the same central density and sound speed  $a$ . The dot-dashed vertical lines mark twice this critical radius. The time for the leftmost pair is half of the collapse time  $\tau_{\text{coll}}$ . The time for the second and third pairs are when the shock reaches the critical BE radius and twice that value. The time for the last pair is the instant of collapse  $\tau_{\text{coll}}$  (defined in the simulations as  $\rho_c/\rho_0 = 4 \times 10^7$ ). The top-right panel shows with a dashed diagonal line the LP density profile  $D = 8.86\xi^{-2}$ .

#### 4. CONVERGING-FLOW MODEL RESULTS

In this section, we present the results of our simulations of core formation and evolution for the case of converging spherical, supersonic flows. For these simulations, the outer boundary condition at  $\xi_{\text{max}}$  is maintained at a constant density and inflow velocity. The inflow velocity is characterized by the Mach number relative to the isothermal sound speed,  $M_a \equiv v_{\text{in}}/a$ . We vary  $M_a$  over the range from 1.05 to 7. For some models (see below), we suppress inflow at the outer radius after collapse occurs to test how the late-time accretion rate is altered. The initial conditions consist of uniform (low) density, and uniform inflow velocity equal to the value at the outer boundary. The size of the grid, in terms of the reference length scale given in Equation (13), is  $2.51327r_0$ , which amounts to a fraction 0.4 of the Jeans length at the initial density. Note that the radius of a critical BE sphere at the same external pressure (so that  $\rho_{\text{edge}} = \rho_0$ ) would be  $R_{\text{BE,crit}} = 6.45(\rho_{\text{edge}}/\rho_c)^{1/2}r_0 = 1.72r_0$ . That is, a critical BE sphere confined by the same ambient pressure would be able to fit within our simulation domain, with plenty of room to spare. The size of zones in the radial direction has a constant logarithmic increment, i.e.,  $\Delta r_{i+1} = (1+\alpha)\Delta r_i$ , for some  $\alpha > 0$ , such that  $r_i = r_1 + \alpha^{-1}[(1+\alpha)^{i-1} - 1]\Delta r_1$  and  $\Delta r_1/(r_{\text{max}} - r_{\text{min}}) = \alpha[(1+\alpha)^{N-1} - 1]^{-1}$ . For all the converging-flow simulations in this paper,  $\alpha$  is set to 0.009; 605 and 597 grids are used during the collapse phase and accretion phase, respectively.

##### 4.1. Core Formation and Collapse

We begin with a description of the core formation process, which is similar for all of the converging-flow models. Because

of the reflecting boundary condition at the center and the initial inflow velocities, immediately after we initiate the simulation, a shock forms at the origin and propagates outward. The inflowing matter is compressed by the shock. The shock front divides the converging inflow into two regions: an inner dense post-shock region and an outer low-density region of supersonic inflow. These two regions evolve quasi-independently but are connected by shock jump conditions. Under competition between gas pressure and self-gravity, the inner region contracts slowly to begin forming a dense core. As self-gravity starts to overwhelm gas pressure, the dense core enters the collapse phase.

At the beginning, the inner region is quasi-hydrostatic, with the velocity a linear function of radius. With negligible density gradient and self-gravity in the early stages, Equation (16) becomes

$$\frac{\partial u}{\partial \tau} + u \frac{\partial u}{\partial \xi} \approx 0. \quad (20)$$

This equation is satisfied by

$$u = \frac{\xi}{\tau - \tau_0}; \quad (21)$$

for  $|\tau/\tau_0| \ll 1$ ,  $u \approx -\xi/\tau_0$ , i.e., the coefficient of the linear profile is constant in time. The leftmost lower panels of Figures 2–5 show this linear-velocity behavior in the shocked region, at the time that equals half of the collapse time  $\tau_{\text{coll}}$ . Throughout this paper, we define the collapse time  $\tau_{\text{coll}}$  as the moment that  $\rho_c/\rho_0 = 4 \times 10^7$ . Shown in the leftmost upper panels of Figures 2–5 are the density profiles; even when the density profile has nonzero gradients, the velocity in the inner

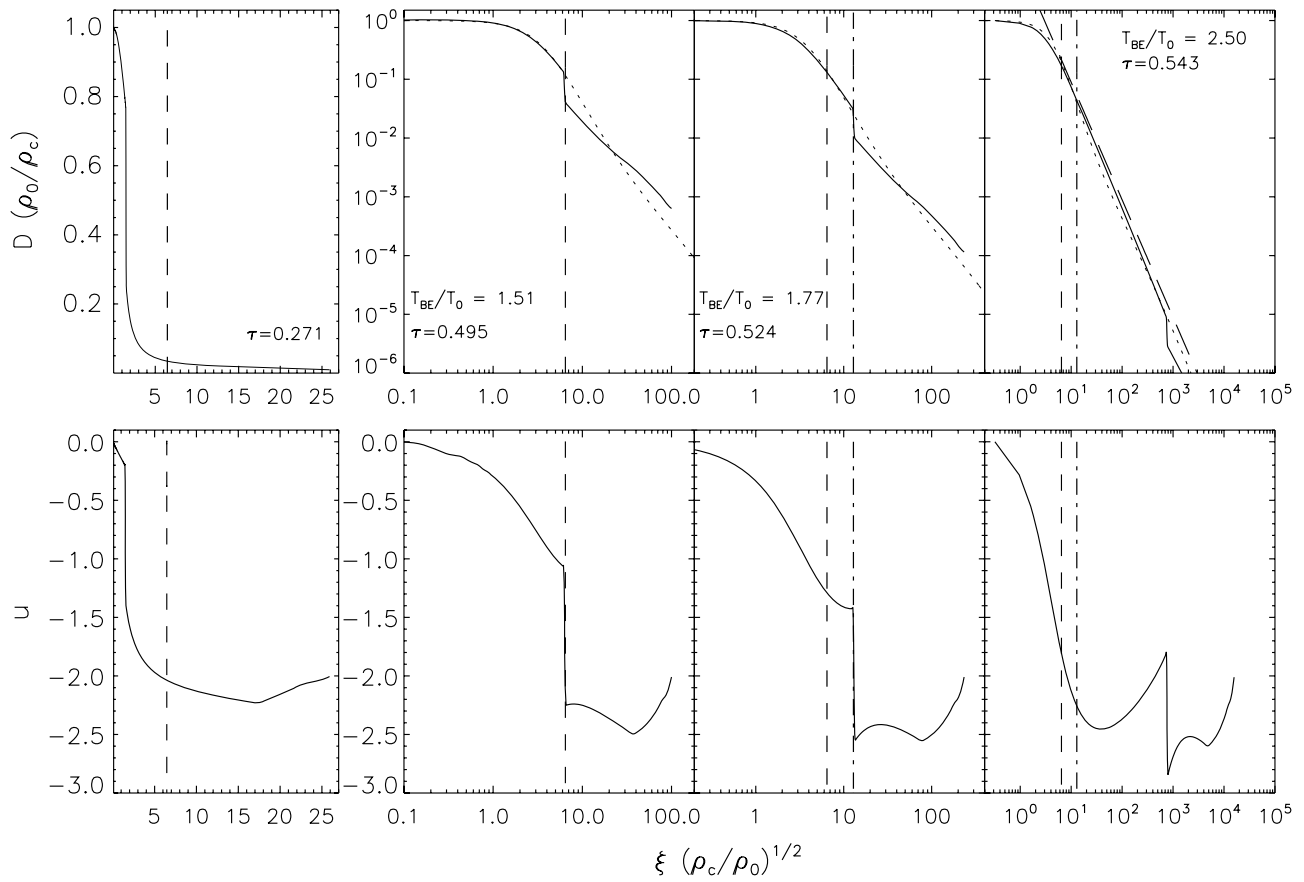


Figure 3. Same as Figure 2, for inflow Mach number  $M_a = 2.0$ .

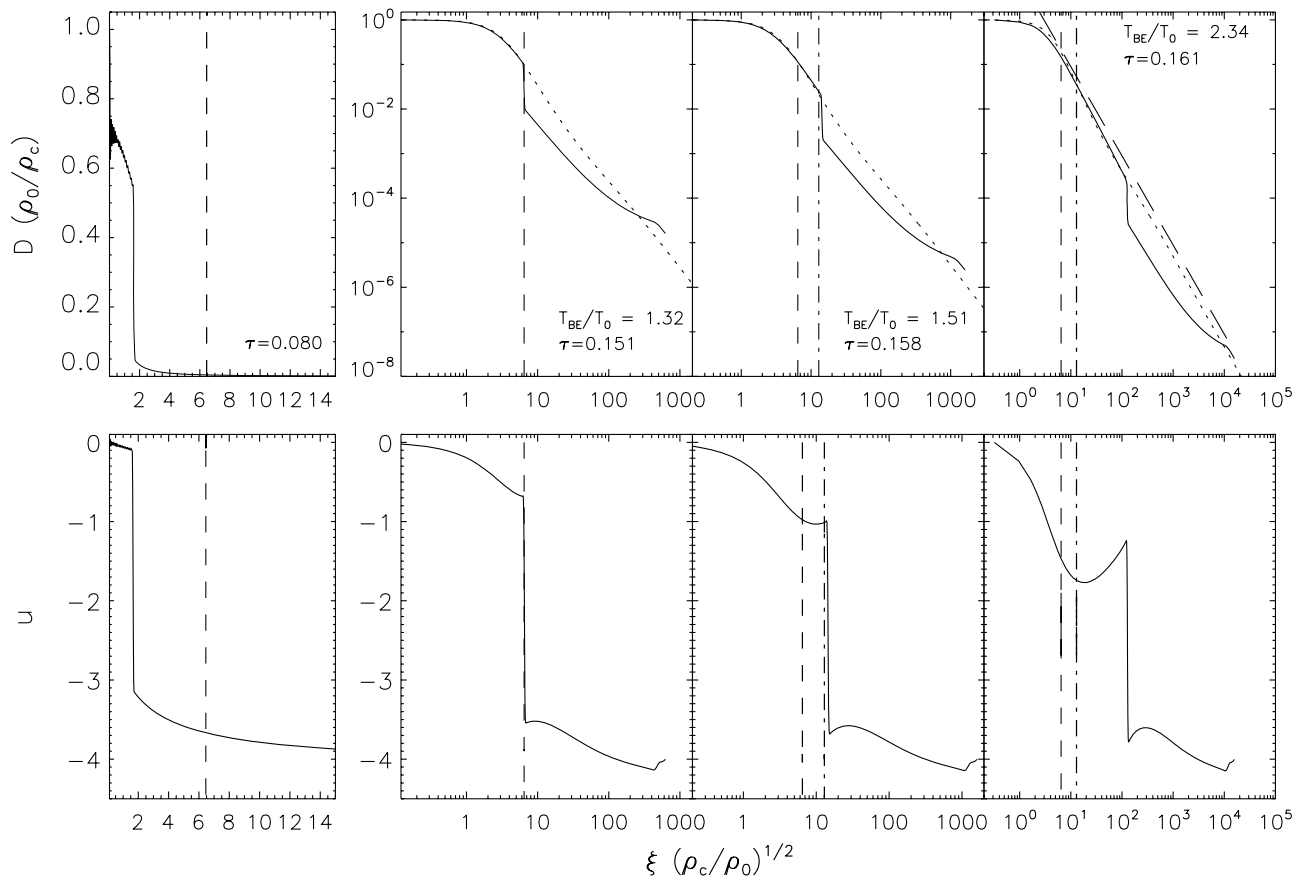
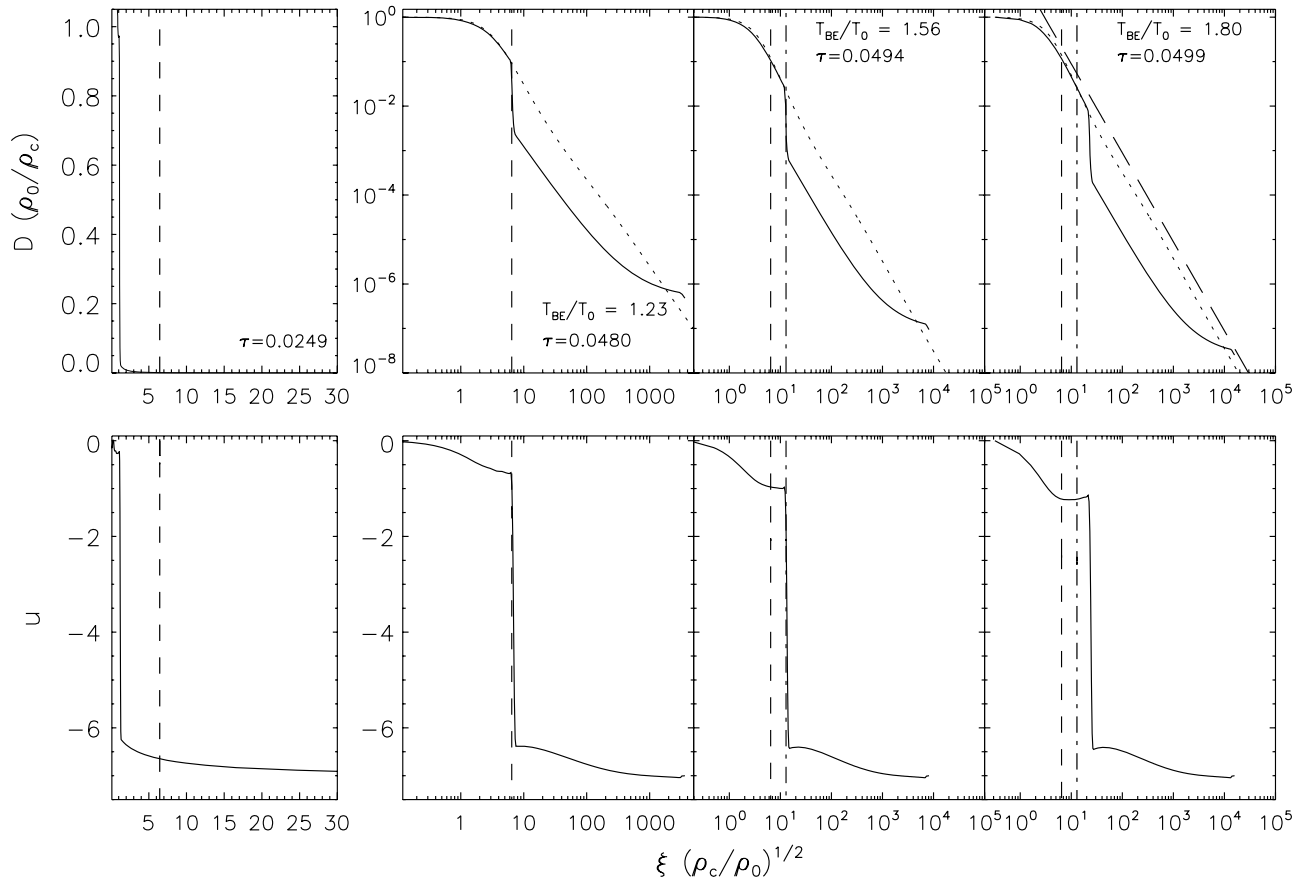


Figure 4. Same as Figure 2, for inflow Mach number  $M_a = 4.0$ .



**Figure 5.** Same as Figure 2, for inflow Mach number  $M_a = 7.0$ .

region is dominated by the linear term. Note that the leftmost panels have linear-linear scales. The velocity over the whole post-shock region is subsonic and negative, which means the core is slowly contracting. For the  $M_a = 4, 7$  models (see Figures 4 and 5), the inner part of the density and velocity profiles oscillate at the beginning of simulations. As the shock front propagates outward, the mass inside the shock increases, and so does self-gravity. After a period of accumulation lasting about 90% of the time until collapse  $\tau_{\text{coll}}$ , the slowly contracting dense region starts to be gravitationally unstable.

Note that the density and velocity profiles of the regions outside of the shock go through a transient evolution after simulations begin. The density profile evolves from a uniform profile set in the initial condition to a  $\rho \propto r^{-2}$  profile consistent with supersonic radial inflow;<sup>2</sup> the material is also increasingly accelerated by gravity. In Figures 2–5, the inflection feature in the velocity profiles exterior to the shock corresponds to a wave propagating inward at a speed equal to the inflow speed plus the sound speed.

Since post-shock velocities are subsonic, gravitational instability is expected to develop at a point when the radius of the inner dense post-shock region becomes comparable to the critical radius of a BE sphere. This expectation is indeed borne out by our simulations, which moreover show that the properties of the collapsing dense inner region are similar as those of collapsing cores initialized from hydrostatic BE spheres. The collapse follows an “outside-in” pattern, starting from the shock front. The

central density increases dramatically and the inflow velocity inside the shock becomes supersonic. The collapse propagates inward and establishes a centrally concentrated density profile (Larson 1969; Penston 1969; Hunter 1977; Shu 1977), which approaches the LP density profile  $D(\xi) = 8.86\xi^{-2}$ , and the velocity approaches  $-3.28a$ .

The three panels on the right of Figures 2–5 show the density profile (top) and the velocity profile (bottom) at three different instants during the outside-in collapse. The density profiles plotted are normalized by the central density and the interior regions are fit by BE sphere density profiles.<sup>3</sup> The ratio between the fitted BE sphere temperature  $T_{\text{BE}}$  and the true temperature  $T_0$  is also noted in the figures. The first figure of these three shows profiles at the instant when the radius of the post-shock region reaches the critical radius (see Equation (18)) of a BE sphere at temperature  $T_0$  with the same central density, i.e.,  $r_{\text{shock}} = R_{\text{BE,crit}}$ . We define the period after this as the supercritical regime. The center-to-edge density ratio after this point exceeds  $\sim 10$ . The second figure of these three shows the instant when the radius of the post-shock region reaches twice the critical radius of a BE sphere. The third figure is at the instant of core-collapse  $\tau_{\text{coll}}$  (defined here as  $\rho_c/\rho_0 = 4 \times 10^7$ ). The long dashed diagonal line in the third figure shows the LP density profile, which is very close to the numerical solution. The time interval between  $r_{\text{shock}} = R_{\text{BE,crit}}$  and collapse for the  $M_a = 2$  case in code units is 0.048 (see Equation (12)), which

<sup>2</sup> For supersonic radial flow,  $v \sim \text{const.}$  upstream of the shock combines with the steady state mass inflow condition  $\rho v r^2 = \text{const.}$  to yield  $\rho \propto r^{-2}$ .

<sup>3</sup> That is, we match solutions of the density profile inside the shock to solutions of the hydrostatic equation  $\frac{d \ln D}{d \xi} = -\frac{m(\xi)}{\xi^2}$  with a fitted temperature  $T_{\text{BE}}$ . These fits are further discussed below.

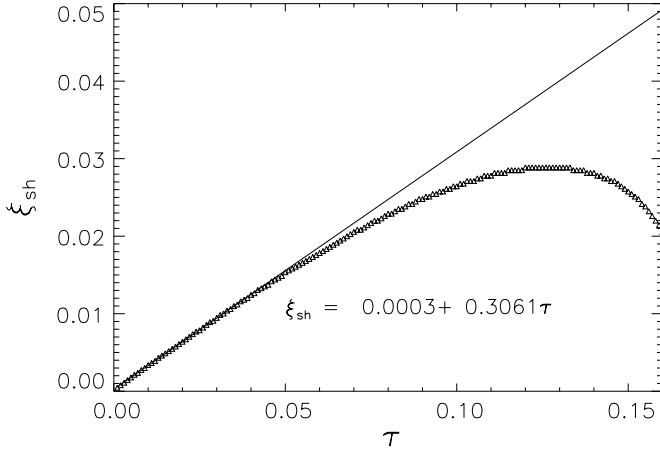


**Figure 6.** Shock front position vs. time for  $M_a = 4$ . The solid line is the best fit to the linear part, i.e., a constant-speed outward-propagating shock at early times. The collapse occurs for this model at  $\tau_{\text{coll}} = 0.16$ .

corresponds to  $1.1 \times 10^5$  yr if the inflowing ambient medium's density is  $n_H = 100 \text{ cm}^{-3}$ .

We note that prior to collapse, the velocities in the dense gas (inside the shock) remain small. In particular, for  $M_a \geq 2$  cases, the inflow velocity inside the shock is subsonic throughout the post-shock region before the time when  $r_{\text{shock}} = R_{\text{BE,crit}}$ . When  $M_a$  is high, Figures 4 and 5 show that the post-shock velocities remain subsonic until shortly before the instant of collapse.

The outward propagation speed of the shock, which from the simulations is approximately constant (Figure 6) at early time, can be obtained using the shock jump conditions. If the shock position is  $\xi_{\text{sh}} = u_{\text{sh}}\tau$ , then provided Equation (21) is satisfied, the velocity on the downstream side is

$$u_d = \frac{\tau u_{\text{sh}}}{\tau - \tau_0}. \quad (22)$$

Note that in order for the downstream velocity to be inward and the shock to be propagating away from the origin, we must have  $\tau < \tau_0$ . The isothermal shock jump conditions, with subscript “ $u$ ” denoting upstream and “ $d$ ” downstream values, are  $D_d(u_d - u_{\text{sh}}) = D_u(u_u - u_{\text{sh}})$  and  $D_d[1 + (u_d - u_{\text{sh}})^2] = D_u[1 + (u_u - u_{\text{sh}})^2]$ ; together these imply  $D_d/D_u = (u_u - u_{\text{sh}})^2$  and  $(u_d - u_{\text{sh}})(u_u - u_{\text{sh}}) = 1$ . Treating the shock speed as approximately constant so that Equation (22) holds, we can solve for the shock velocity to obtain  $u_{\text{sh}} = \frac{1}{2}(u_u + [u_u^2 + 4 - 4(\tau/\tau_0)]^{1/2})$ . For  $\tau/\tau_0 \ll 1$ , and taking the upstream velocity as  $u_u \approx -M_a$  which corresponds to the limit of strongly supersonic inflow, gives

$$u_{\text{sh}} \approx \frac{1}{2}[-M_a + (M_a^2 + 4)^{1/2}] = \frac{2}{M_a + (M_a^2 + 4)^{1/2}}. \quad (23)$$

The shock speed decreases as the Mach number increases, and therefore from Equation (22) the post-shock flow speed also decreases as the Mach number increases. Figure 6 shows the position of shock front versus time for  $M_a = 4$ . The intercept and the slope are based on the best fit of the linear part where  $\tau \in [0.0, 0.04]$ . The intercept is nearly 0 and the slope 0.3061 is the measured shock speed in units of the isothermal sound speed  $a$ ; Equation (23) predicts a slightly smaller value 0.24. The analytical solution (Equation (23)) for  $u_{\text{sh}}$  as a function of  $M_a$  is plotted as a dotted line in Figure 7 (labeled as  $u_{\text{sh,estimate}}$ ) and the shock speeds directly measured from simulations  $u_{\text{sh}}$

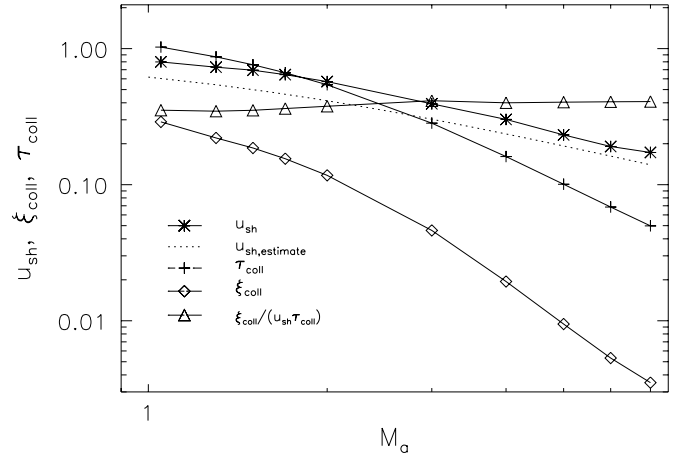


**Figure 7.** Speed of shock front at early times (asterisks), the radius of the core at the instant of collapse (diamonds), and the time at which collapse occurs (plus signs) as a function of  $M_a$ . Triangles show the ratio of  $\xi_{\text{coll}}/(u_{\text{sh}}\tau_{\text{coll}})$ , which is nearly constant, ranging from 0.34 to 0.42. The dotted line is the analytic estimate for  $u_{\text{sh}}$  given in Equation (23).

are plotted as asterisks. The analytical approximation is about 15%–28% below the measured value from the simulations as  $M_a$  ranges from 1.05 to 7.0.

Using the constant-shock-speed approximation, the immediate post-shock density can also be obtained in terms of the pre-shock density, in the limit  $\tau/\tau_0 \ll 1$  and using  $u_u \approx -M_a$  as

$$\frac{D_d}{D_u} = \frac{1}{4} [M_a + (M_a^2 + 4)^{1/2}]^2, \quad (24)$$

which for  $M_a \gg 1$  is  $D_d/D_u \approx M_a^2$ . Because of the radial convergence of the inflow in the simulations,  $D_u$  varies; it is initially equal to 1, but after an initial transient, in the highly supersonic limit  $D_u$  would approach  $(\xi_{\text{outer}}/\xi_{\text{sh}})^2$  because of mass conservation.

It is interesting to investigate how the state of the core when it collapses depends on Mach number. Figure 8 shows the density profiles and the velocity profiles of the simulated cores at the instant of collapse  $\tau_{\text{coll}}$ , for different Mach numbers. First, it is clear that all the density profiles approach the LP solution, especially for low Mach number cases. The inflow velocity inside the shock is supersonic and does not strongly vary over the dense core region. The smaller the Mach number is, the closer the inflow speed is to the LP result,  $v = -3.3a$ . Second, the radius of the core at the instant of collapse decreases as Mach number increases. We plot this dependence in Figure 7 with diamonds.

We quantitatively compare the basic core properties in Figure 7, which shows the collapse time  $\tau_{\text{coll}}$  and the shock radius  $\xi_{\text{coll}}$  at time  $\tau_{\text{coll}}$ , both as function of  $M_a$ . As noted above,  $\xi_{\text{coll}}$  decreases with increasing  $M_a$ ; the same is true for  $\tau_{\text{coll}}$ . We also recall that  $u_{\text{sh}}$  decreases with  $M_a$ . Interestingly, while  $\xi_{\text{coll}}$ ,  $u_{\text{sh}}$ , and  $\tau_{\text{coll}}$  all decrease with  $M_a$ , the ratio  $\xi_{\text{coll}}/(u_{\text{sh}}\tau_{\text{coll}})$  is nearly constant with  $M_a$ : it ranges only from 0.34 to 0.42 (see Figure 7). This result is potentially useful for empirical estimates of core lifetimes, since the inflow velocity  $M_a$ , the isothermal sound speed  $a$  and the radius of dense core are all in principle measurable. If the ratio  $\xi_{\text{coll}}/(u_{\text{sh}}\tau_{\text{coll}})$  is taken as a constant  $\approx 0.4$ , and the shock speed is estimated via Equation (23), then the lifetime of cores up to the point of collapse is given in dimensional form by  $t_{\text{coll}} \approx 1.3R_{\text{coll}}[M_a + (M_a^2 + 4)^{1/2}]/a$ . In practice, it may be difficult to measure  $M_a$  outside of a core,



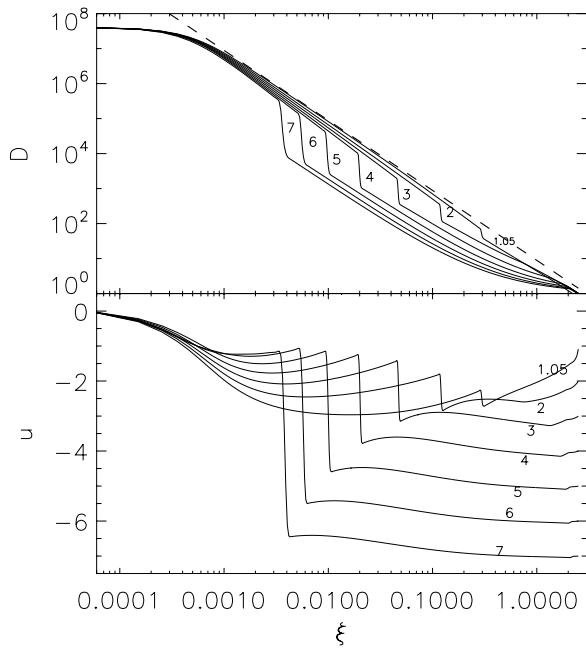


**Figure 8.** Density profiles (top panel) and the velocity profiles (bottom panel) at the instant of collapse for simulations with different Mach number  $M_a$  (as labeled). The thick dashed line in the top panel is the LP density profile  $D = 8.86\xi^{-2}$ . For higher  $M_a$  cases, the shock front is at smaller radius (in units of  $r_0$ ) and the post-shock speeds in the dense core are lower in magnitude. Units of length and velocity are given by Equations (13) and (11), respectively. The density is in units of the GMC ambient value.

because the density is much lower than that of the core, and it is difficult to isolate the immediate environment of the core from foreground and background gas. This result is still useful in a statistical sense, however, using the mean Mach number of the turbulent flow in a cloud.

Another direct observable is the core density, so it is interesting to test how the values of the collapse time and radius depend on the mean density in the core at the time of collapse. Diamonds in the top panel of Figure 9 show the core radius in units of  $a(4\pi G\rho_{\text{mean}})^{-1/2}$ , which is  $\xi_{\text{coll}}(\rho_{\text{mean}}/\rho_0)^{1/2}$ , as a function of  $M_a$ . We can see  $\xi_{\text{coll}}(\rho_{\text{mean}}/\rho_0)^{1/2}$  is nearly constant, ranging from 4.58 to 3.42 as Mach number increases from 1.05 to 7. Taking this as approximately constant, and using the measured core mean density, the predicted size of core at the time of collapse is  $R_{\text{coll}} \approx 4a(4\pi G\rho_{\text{mean}})^{-1/2}$ . Note that this radius is  $\sim 50\%$  larger than the critical BE radius for the same temperature (see Equation (18)). Since the post-shock density increases relative to the upstream density approximately as  $D_d/D_u \sim M_a^2$  (see Equation (24)), it is also interesting to test how  $\xi_{\text{coll}}M_a$  depends on Mach number. In fact this quantity decreases with  $M_a$ , as seen in Figure 9.

To express the core-collapse time in terms of observables, we normalize the collapse time using the mean core density. This quantity  $t_{\text{coll}}(4\pi G\rho_{\text{mean}})^{1/2} = \tau_{\text{coll}}(\rho_{\text{mean}}/\rho_0)^{1/2}$  is plotted in Figure 9 as a function of  $M_a$ . For reference, the core-collapse time normalized using  $M_a$  is also plotted in Figure 9. The free-fall time  $t_{\text{ff}}$  for a uniform sphere in units of  $(4\pi G\rho_{\text{mean}})^{-1/2}$  is 1.92, so that we have  $t_{\text{coll}} \sim 8\text{--}26 t_{\text{ff}}$  as Mach number varies from 1.05 to 7. This timescale is much longer than the observed values  $\sim 2\text{--}5 t_{\text{ff}}$  for prestellar cores. The reason for this disparity is that during the early part of its evolution, the central density of the core is low, and it would not be identifiable within its surroundings. This is evident in

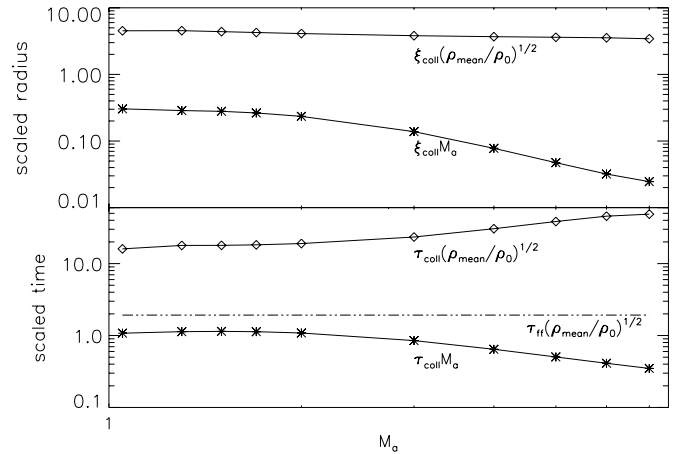


**Figure 9.** Renormalized radius (top panel) and collapse time (bottom panel) of cores vs.  $M_a$ . Diamonds show quantities normalized using the mean core density and asterisks show quantities normalized using the Mach number (see the text). The dot-dashed line in the lower panel shows the free-fall time at density  $\rho_{\text{mean}}$  in units  $(4\pi G\rho_{\text{mean}})^{1/2}$ , i.e.,  $\tau_{\text{ff}}(\rho_{\text{mean}}/\rho_0)^{1/2} = \pi(3/8)^{1/2}$ .

the low contrast between the center and the edge of the core seen in the first frames of Figures 2–5. Only when the core approaches collapse does the center-to-edge contrast become large. For example, for the  $M_a = 1.05$  model, the center-to-edge density ratio  $\rho_c/\rho_{\text{edge}}$  reaches 2 at  $\tau = 0.78$  and reaches 5 at  $\tau = 0.92$ ; this can be compared with the total time until collapse,  $\tau_{\text{coll}} = 1.027$  for this model. For the whole set of models, the observable fraction of the pre-collapse core life is 30%–50% if we choose  $\rho_c/\rho_{\text{edge}} \geq 2$ , or 10%–20% if we choose  $\rho_c/\rho_{\text{edge}} \geq 5$ . Taking the period when  $\rho_c/\rho_{\text{edge}} \geq 2$  or  $\rho_c/\rho_{\text{edge}} \geq 5$  as the period over which a core could be observable, e.g., in submillimeter continuum, our simulations give  $t_{\text{observable}} \sim 2\text{--}13 t_{\text{ff}}$  or  $t_{\text{observable}} \sim 1\text{--}6 t_{\text{ff}}$ , respectively. The latter is consistent with observed estimates.

Another observable aspect of prestellar cores is their density structure. As discussed above, for each solution at the times shown in Figures 2–5, we fit a BE sphere profile. The density in code units  $\rho_0$  is  $D(\xi) = \rho/\rho_0$  and the radius in code units is  $\xi = r(4\pi G\rho_0)^{1/2}/a$ . When the central density is instead used to normalize, the density and radius variables are

$$\tilde{D} = \rho/\rho_c = D\rho_0/\rho_c \quad (25)$$

and

$$\tilde{\xi} = r \frac{(4\pi G\rho_c)^{1/2}}{a} = \xi(\rho_c/\rho_0)^{1/2}. \quad (26)$$

For a BE sphere with sound speed  $a_{\text{BE}}$ , the density profile normalized by the central density is  $\tilde{D}_{\text{BE}}$ , which is a function of the scaled radius  $\xi_{\text{BE}} = r(4\pi G\rho_c)^{1/2}/a_{\text{BE}} = \tilde{\xi} a/a_{\text{BE}}$ . To fit the density profiles in our simulations to a BE sphere, the only free parameter is the ratio of the isothermal sound speed  $a_{\text{BE}}$  of the BE sphere to the sound speed in the simulations,  $a$ . Thus, for any given density profile  $\tilde{D}$  we adjust the value of  $a_{\text{BE}}/a$  until a good match between  $\tilde{D}_{\text{BE}}$  and  $\tilde{D}$  is obtained. This procedure yields the fitted temperature ratio:

$$\frac{T_{\text{BE}}}{T_0} = \left(\frac{a_{\text{BE}}}{a}\right)^2. \quad (27)$$

The values obtained for  $T_{\text{BE}}/T_0$  are marked in Figures 2–5. The range of values we find is 1.23–2.89. This range is consistent with theoretical expectations. As the radius of the

BE sphere extends to infinity, the density profile approaches the singular solution  $\rho = 2a_{\text{BE}}^2/(4\pi Gr^2)$  (Shu 1977) corresponding to  $\bar{D}_{\text{BE}} = \rho/\rho_c = 2(a_{\text{BE}}/a)^2\tilde{\xi}^{-2}$ . The density profile of the collapsed core approaches the LP solution  $\bar{D} = 8.86\tilde{\xi}^{-2}$ . To match the LP profile with the singular profile therefore requires  $2(a_{\text{BE}}/a)^2 = 8.86$ , which corresponds to a temperature ratio  $T_{\text{BE}}/T_0 = 8.86/2 = 4.43$ . Fits of core profiles to BE spheres that indicate values of  $T_{\text{BE}}$  up to 4.43 times the measured thermal temperature therefore are expected if collapse has taken place; this does not by itself indicate that magnetic support is present.

#### 4.2. Post-Collapse Evolution: Infall and Accretion Stages

After the central density becomes singular, the evolution transitions to the infall and accretion stages. For our simulations, we make this transition by implementing an outflow boundary condition at the center when the central density reaches  $4 \times 10^7 \rho_0$ . The initial mass of the central protostar is calculated by integrating the innermost part of the density profile where density is between  $[1 \times 10^7, 4 \times 10^7] \rho_0$ . The specific choice of this density does not significantly affect  $\tau_{\text{coll}}$ ,  $\xi_{\text{coll}}$ , or the subsequent evolution since the central density increases dramatically only at the very end of the collapse stage.

At the beginning of the accretion phase, the material inside the shock falls onto the protostar. The material approaching the protostar is in a free-fall state (Hunter 1977). The region of unsupported infall starts from the center and propagates outward, similar to the “expansion wave” described by Shu (1977). The density profile inside the rarefaction wave changes from  $\rho \propto r^{-2}$  to  $r^{-3/2}$  and the velocity profile changes from  $v \propto r^0$  to  $r^{-1/2}$ . For our simulations, this infall stage ends as the infall rarefaction wave arrives at the shock front. This generally occurs very rapidly (in less than 10% of  $\tau_{\text{coll}}$ ; see below).

For an initially static density profile  $Ar^{-2}$ , where  $A = Ka^2/(4\pi G)$  and  $K$  is a constant, if the gas pressure is negligible the average speed of the rarefaction wave is  $(2\sqrt{2K}/\pi)a$ . For  $K = 8.86$ , which is the LP profile, this yields  $2.7a$ . For the real case, the initial velocity is nonzero and the gas pressure is nonnegligible, so that the rarefaction wave propagates at a modified speed. For example, for the  $M_a = 1.05$  model, which has  $\xi_{\text{coll}} = 0.29$  and infall interval  $\Delta\tau_{\text{inf}} = 0.092$ , the average speed is  $3.15a$ . For  $M_a = 4.0$  and  $7.0$ , the measured average infall speed of the infall rarefaction wave is  $2.22a$  and  $1.95a$ , respectively.

After the infall rarefaction wave arrives at the shock front, the final accretion stage begins, with material initially outside the shock falling onto the protostar at supersonic speeds. This process is similar to Bondi accretion, except that the central mass is growing and the velocity field for our simulations is uniformly converging at large distance. During this stage, the density and the velocity profiles vary  $\propto r^{-3/2}$  and  $r^{-1/2}$ , respectively, corresponding to free fall.

The typical density profiles and velocity profiles during the accretion stage for  $M_a = 1.05$  and 4 models are shown in Figure 10. Three different instants in the evolution are shown: the instant of core collapse, the instant when the infall rarefaction wave arrives at the shock front, and a point during the late accretion stage. The transition from the LP profiles to the free-fall profiles in density and velocity are clearly evident in the figure.

In a real system, the duration of the accretion stage depends on the environment of the protostar, and how long the inflow that creates the core is maintained at large scales. To explore how the late-time evolution is affected by changes in the accretion, we have conducted additional simulations in which

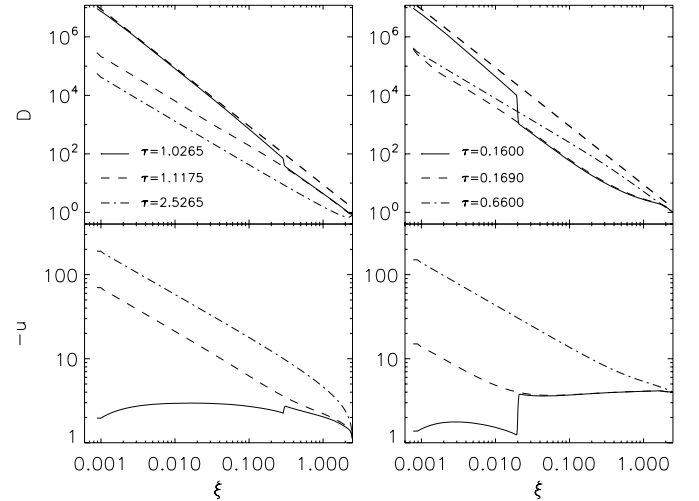


**Figure 10.** Density and velocity profiles during the accretion phase for  $M_a = 1.05$  (left) and  $M_a = 4$  (right) models. The density profiles (top) and the velocity profiles (bottom) are each shown at three different instants: the solid lines show the instant of core collapse, the dashed lines show the instant when the gravitational rarefaction wave arrives at the shock front, and the dot-dashed lines show the profiles at a late accretion stage. Numbers in the figure show the corresponding time for each instant. In the upper panels, the LP density profile  $D = 8.86\xi^{-2}$  is plotted for reference with the thick dashed lines. The transitions from  $D \propto \xi^{-2}$  (early) to  $D \propto \xi^{-3/2}$  (late) and  $u \propto \xi^0$  (early) to  $u \propto \xi^{-1/2}$  (late) are evident.

the flow inward from the outer boundary is halted at the end of the infall stage (i.e., when the rarefaction reaches the shock). Suppression of inflow will affect the mass flux onto the protostar after the rarefaction wave from the boundary reaches the central protostar. We discuss comparison of these models to our standard models in Section 4.4.

#### 4.3. Definition of Evolutionary Stages

Based on the results presented in Sections 4.1 and 4.2, we have identified four main stages of protostellar core formation and evolution in a supersonic turbulent medium (see Figure 11 for a schematic depiction).

1. *Core building.* Converging flows in a supersonic turbulent medium collide, with post-shock compressed gas accumulating over time in stagnant, shock-bounded regions. If these dense regions are not destroyed by larger-scale turbulence, the high-density gas will undergo a long contraction process during which gas pressure competes with self-gravity. The typical character of this stage is that the velocity inside the dense gas is subsonic and increases linearly with distance from the center. Since the center-to-edge density contrast is relatively low, these clumps are gravitationally subcritical. Toward the end of this stage, when the center-to-edge density contrast becomes appreciable, these objects would become observable as prestellar cores. This core-building stage lasts  $>90\%$  of  $\tau_{\text{coll}}$ ; only the last 10%–20% would be observable.
2. *Core collapse.* The core built up during the first stage accumulates enough mass that it becomes gravitationally supercritical, which we operationally define as  $r_{\text{shock}} > R_{\text{BE,crit}}$ . Self-gravity overwhelms the gas pressure, and the unstable core starts to collapse. The collapse begins near the shock front, where the imbalance between gravity and pressure gradient forces is greatest, and propagates inward. This collapse is an “outside-in” process. During

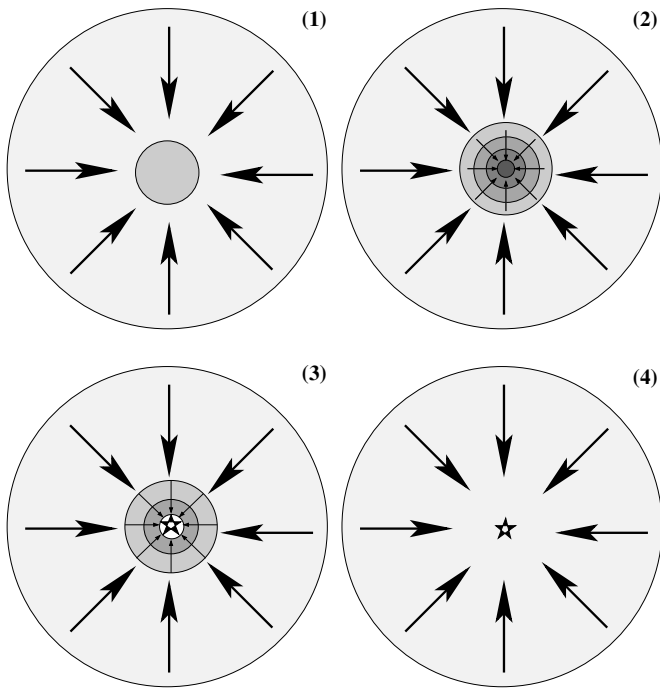


**Figure 11.** Four stages of core evolution in the idealized models of this paper. (1) Core building via supersonic converging flow, yielding a stagnant, shock-bounded dense region. (2) Core collapse, propagating from outside to inside, leading to a density profile  $\rho \propto r^{-2}$ . (3) Envelope infall, propagating from inside to outside, and resulting in free fall onto the protostar. (4) Late accretion of ambient gas onto the protostar. For real systems, evolution would be modified in several ways: converging flows would be nonspherical, angular momentum would lead to disk formation, and outflows would contribute to clearing the envelope.

core collapse, the central density increases dramatically and the inflow velocity inside the core becomes supersonic. As the collapse propagates inward, a density profile  $\rho \propto r^{-2}$  is left behind and the velocity increases toward the center. The end of this stage is defined by the instant of protostar formation  $\tau_{\text{coll}}$ , when the wave of collapse has reached the center of the core. The density profile approaches the LP profile,  $\rho = 8.86a^2/(4\pi Gr^2)$ . The velocity in the interior of the collapsed core approaches a uniform value comparable to that in the LP solution  $-3.28a$ . The central density is high enough to be optically thick and a protostar forms. Because of their large central volume densities, prestellar cores during this collapse stage would be observed as having high peak submillimeter flux densities. This stage lasts for a time  $\Delta\tau_{\text{supercrit}}$ , less than 10% of the prestellar core lifetime  $\tau_{\text{coll}}$ .

3. *Envelope infall.* During this stage, the high-density material inside the shock front falls to the protostar (or, if angular momentum was included, a circumstellar disk). This stage starts at the instant of the protostar formation and ends at the instant when the gravitational rarefaction wave reaches the shock front, clearing out the remnants of the dense gas that accumulated during core building. During this stage, the density and velocity profiles in the interior change from LP profiles to free-fall profiles. Since the core contains an embedded protostar, the system would be observationally classified as Class 0/I. This stage lasts for a time  $\Delta t_{\text{infall}}$  less than 10% of the prestellar core lifetime. In a real system, the fraction of the envelope mass that eventually reaches the center would depend on the details of the protostellar wind, which would sweep up at least the polar portion of the envelope, creating an outflow.

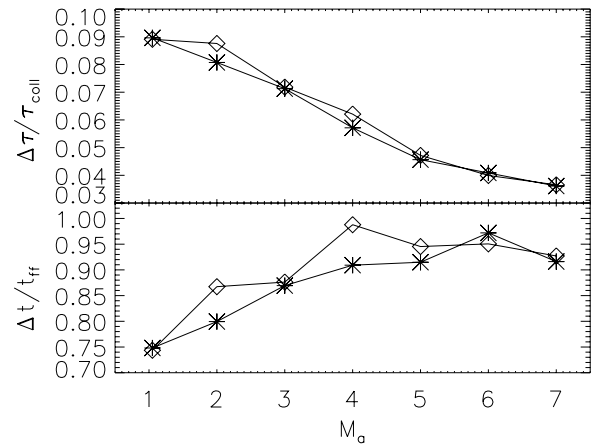


**Figure 12.** Top panel shows the ratio of the duration of the supercritical collapsing stage  $\Delta\tau_{\text{supercrit}}$  (asterisks) and the post-collapse infall stage  $\Delta\tau_{\text{infall}}$  (diamonds) to the prestellar lifetime  $\tau_{\text{coll}}$  of cores, as a function of Mach number. The bottom panel shows ratios  $\Delta t_{\text{supercrit}}/t_{\text{ff}}$  (diamonds) and  $\Delta t_{\text{infall}}/t_{\text{ff}}$  (asterisks), which range from [0.8, 1], as a function of Mach number; here  $t_{\text{ff}}$  is computed using the mean density inside the shock at  $\tau_{\text{coll}}$ .

4. *Late accretion.* During this stage, material from the ambient environment directly accretes to the protostar (or, more realistically, a disk). Accretion during this stage is similar to Bondi accretion, with free-falling density and velocity profiles  $\rho \propto r^{-3/2}$  and  $v \propto r^{-1/2}$  over the whole core region. For a real system, the duration of the late accretion stage, and hence the final stellar mass, depends on ambient conditions far from the protostar. In a real system, the potential of this stage to contribute significantly to the stellar mass would also depend on protostellar winds, which can reverse the accretion.

Although we have identified these stages based on idealized spherically symmetric models with constant gaseous inflow rates at large distance, we expect that the same stages would be present, in modified form, under more realistic conditions. Based on our simulations, the ratios  $\Delta\tau_{\text{supercrit}}/\tau_{\text{coll}}$  and  $\Delta\tau_{\text{infall}}/\tau_{\text{coll}}$  decrease with increasing  $M_a$ , as shown in Figure 12. The supercritical stage and the infall stage have similar durations, and range from 9% to 3% of the prestellar core lifetime  $t_{\text{coll}}$ , which itself ranges from 8 to 26  $t_{\text{ff}}$ . The supercritical collapse period (stage 2)  $\Delta t_{\text{supercrit}}$  and the infall period (stage 3)  $\Delta t_{\text{infall}}$  thus both range over  $\sim 0.8-1 t_{\text{ff}}$ , as shown in Figure 12. While the time to reach collapse would differ for nonspherical or nonsteady converging large-scale flows, we expect that the character of the evolution would not. We also expect that the ratios  $\Delta t_{\text{supercrit}}/t_{\text{ff}}$  and  $\Delta t_{\text{infall}}/t_{\text{ff}}$  would remain order unity.

#### 4.4. Evolution of Mass Accretion Rates

Figure 13 shows the temporal evolution of the mass accretion rate and the total integrated mass of the central protostar for  $M_a = 1.05, 2, 4$ , and 7. These can be compared with the mass accretion rate and the integrated central mass for an initially static critical BE sphere, as shown in Figure 1 (see also Vorobyov & Basu 2005, who show similar accretion histories to Figure 1). For both the initially static collapse and our models that allow for core building from supersonic flows, there is a sharp early peak in the accretion rate. The rise starting from  $\dot{M} = 0$  corresponds to the moment of protostar formation at  $\tau_{\text{coll}}$ . The smooth decline that follows (ending at the points marked “i” in Figure 13) corresponds to the infall stage, as the gravitational rarefaction wave propagates outward. At late times, however, the accretion

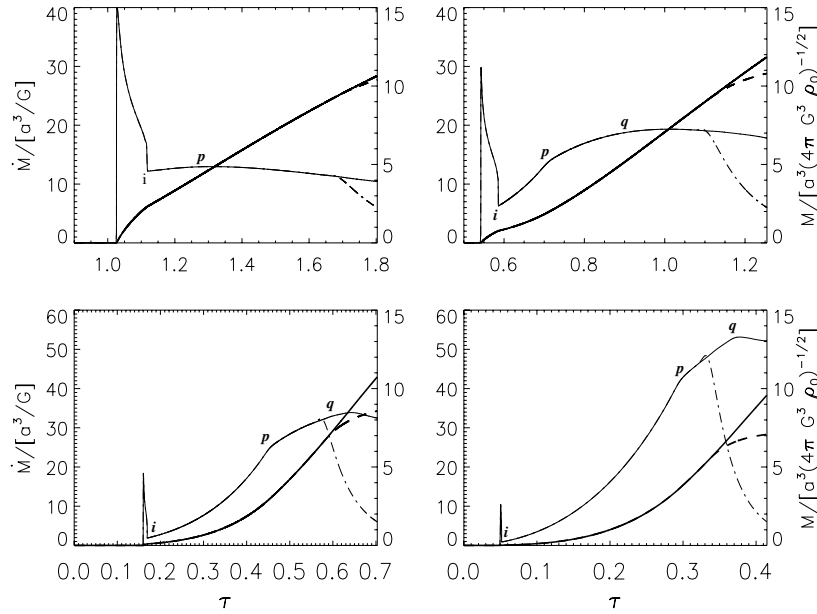


**Figure 13.** Temporal evolution of the mass accretion rate (thin solid lines; left axis) and the integrated mass of protostar (thick solid line; right axis) for models with Mach number  $M_a = 1.05, 2, 4,$  and  $7,$  as labeled. The corresponding dot-dashed lines show the results for models in which the inflow to the grid is suppressed after the end of the infall stage. The point marked  $i$  represents the end of the infall stage,  $p$  represents the instant when the density profile reaches  $\rho \propto r^{-3/2}$  everywhere, and  $q$  represents the instant when the velocity profile reaches  $v \propto r^{-1/2}$  everywhere. Units of time, mass, and accretion rate are given by Equations (12), (14), and (3), respectively.

differs for the initially static versus dynamically built cores. For an initially static unstable BE core, the late accretion steadily declines over time (Figure 1). In contrast, for cores formed in the  $M_a = 1.05$  model (i.e., barely supersonic inflow), the late-time accretion is nearly constant, and for cores formed in large  $M_a$  models, the late accretion rate increases over time (thin lines in Figure 13).

The early-time peak accretion rates can be compared with the predictions of self-similar models. For the LP profiles at the instant of core collapse,  $D = 8.86\xi^{-2}$  and  $u = -3.28$  give  $\dot{M} = 29.1a^3/G$ , while the self-similar solution for the accretion phase in Hunter (1977) predicts  $\dot{M} = 46.195a^3/G$ . In fact, we do see a jump in  $\dot{M}$  above  $29.1a^3/G$  as the evolution transits from the collapse stage to the infall stage. This phenomenon is most clearly evident for the  $M_a = 1.05$  model, which has the highest resolution of the central region because the shock strength is lower than in the high  $M_a$  models, yielding a larger core (see Figure 8) at the instant of collapse.

The detailed behavior of  $\dot{M}$  during the late accretion stage can be understood in terms of various transitions that occur. For  $M_a = 1.05$ , the accretion rate (see Figure 13) starts to increase from point  $i$  until to point  $p$ , and then decreases. The increases from  $i$  to  $p$  occurs as gas stored between the shock front and the outer boundary collapses into the center. The point  $p$  represents the instant when the density in the whole outer region reaches a profile  $\rho \propto r^{-3/2}$ . After point  $p$ , the gravitational rarefaction has reached the boundary, and subsequent accretion is limited by the inflow rate imposed at the outer boundary. For the  $M_a = 2, 4,$  and  $7$  models shown in Figure 13, the mass accretion process between point  $i$  and  $p$  is similar to that of  $M_a = 1.05$ . However, there is additional transitory behavior before the accretion rate decreases to the inflow rate imposed at the boundary. At the instant corresponding to point  $p$ , the rarefaction has produced  $\rho \propto r^{-3/2}$  over the whole region. But the velocity profile has  $v \propto r^{-1/2}$  only over the inner region. During the stage between point  $p$  and  $q$ , the density profile stays almost unchanged but the velocity profile evolves to reach  $v \propto r^{-1/2}$  everywhere (see

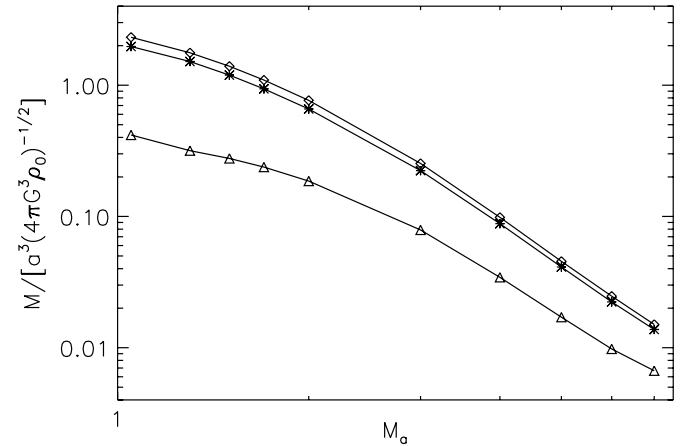


**Figure 14.** Protostellar mass at the end of the infall stage (diamonds), the core mass inside the shock at the instant  $\tau_{\text{coll}}$  of protostar formation (asterisks), and the critical BE sphere mass (triangles) based on the mean core density at time  $\tau_{\text{coll}}$ , all as a function of Mach number  $M_a$ . The mass unit is given by Equation (14).

also Figure 10). After point  $q$ , the accretion rate decreases to the imposed inflow rate. The stage between  $p$  and  $q$  is most obvious for the  $M_a = 4.0, 7.0$  models.

As mentioned above, we have also performed models in which inflow to the grid is halted after the point when the rarefaction reaches the shock. The resulting late-stage accretion (see Figure 13) is initially the same as in our standard models, but then declines over time, after the rarefaction wave reaches the boundary.

The mass of the protostar at the end of the infall stage and the total core mass  $M_{\text{core}}$  inside the shock at instant of core collapse are shown in Figure 14. For comparison, we also show the critical BE sphere mass (see Equation (19)) using the mean core density at the time of collapse for  $\rho_{\text{mean}} = 2.45\rho_{\text{edge}}$ ; these are lower than the actual core mass. Because there is continued mass passing through the shock during the infall



stage, the post-infall protostellar mass is slightly higher than the core mass inside the shock at the time when core collapses. As the Mach number increases, the post-infall protostellar mass and the core mass at  $\tau_{\text{coll}}$  both decrease. The protostellar mass ranges over  $0.06\text{--}8.8 M_{\odot}$  and the core mass at  $\tau_{\text{coll}}$  ranges over  $0.05\text{--}7.5 M_{\odot}$ , taking  $n_H = 100 \text{ cm}^{-3}$  for the ambient density.

## 5. SUMMARY AND CONCLUSIONS

Star formation takes place in GMCs pervaded by supersonic turbulence, and theoretical models of prestellar (and protostellar) cores must take these large-scale supersonic flows into account. Here, we have developed models in an idealized, spherically symmetric framework that nevertheless captures key aspects of the real situation, enabling us to identify and analyze the main stages of core formation and evolution in a dynamic environment.

Our models differ from previous studies of core evolution in that the cores are not present as either stable or unstable density concentrations in our initial conditions—the initial density is everywhere uniform. Instead, during the first evolutionary stage cores are built “from scratch” by the collision of converging supersonic flows. The boundaries defining the outer edge of a core—where the density drops—correspond to a shock front across which the temperature is constant and the mass flux is nonzero. The shock front propagates outward, with the mass of the post-shock dense region growing in time. Initially, the core is essentially uniform. Over time, the mass grows sufficiently so that the core becomes centrally stratified due to self-gravity. Observationally, the latter part of this “core-building” stage corresponds to prestellar cores that have low to intermediate peak brightness. The period over which  $\rho_c/\rho_{\text{edge}} \geq 5$ , and a core would be clearly identifiable in observations, amounts to  $1\text{--}6 t_{\text{ff}}$ , with the free-fall time defined using the mean core density.

When the center-to-edge density contrast exceeds  $\sim 10$ , the core becomes supercritical and a stage of violent “outside-in” collapse ensues. The density profile throughout the core approaches  $\rho \propto r^{-2}$ , and a protostar forms at the center. We define the instant that collapse is complete and a protostar forms as  $t_{\text{coll}}$ , or  $\tau_{\text{coll}}$  in our dimensionless variables. Although the central density becomes very large, the wave of outside-in collapse still leaves most of the core mass in the outer parts. Observationally, this core-collapse stage corresponds to prestellar cores that have high peak brightness. The period  $\Delta t_{\text{supercrit}}$  over which cores are supercritical, undergoing outside-in collapse, amounts to less than 10% of  $t_{\text{coll}}$ , or  $0.8\text{--}1 t_{\text{ff}}$ .

The third stage of evolution is governed by an “inside-out” wave of gravitationally driven rarefaction propagating from the center of the core to the shock front that defines the core’s outer edge. The accretion rate onto the star during this infall stage is initially very high, but declines over time. At the end of this infall stage, the dense envelope built during the first stage has plunged into the star. The velocity and density profiles approach free fall,  $v \propto r^{-1/2}$  and  $\rho \propto r^{-3/2}$ , respectively. Observationally, this stage corresponds to Class 0/I embedded protostars. The period  $\Delta t_{\text{infall}}$  over which cores undergo this inside-out infall is similar to the duration of the previous stage,  $\Delta t_{\text{supercrit}}$ , and comparable to  $t_{\text{ff}}$ .

During the final stage of evolution, there is no longer a massive envelope. The protostar can continue to accrete from the more distant, lower-density gas in its surroundings. The late-stage accretion rate and the total mass accumulated by the system depend on the large-scale environment, rather than the properties established in the core during the building stage.

Observationally, this stage corresponds to a nonembedded YSO that may still be accreting from a disk.

Based on our simulations, our chief conclusions are as follows.

1. The initiation of star formation via outside-in core collapse, followed by inside-out envelope infall, appears to be very robust. The dynamical behavior during these stages of evolution is very similar whether the core is initiated as an unstable equilibrium (as in previous models) or is built up dynamically through a shocked converging flow (as in the present work). The LP singular solution with  $\rho = 8.86a^2/(4\pi Gr^2)$  appears to be an “attractor,” in that models initiated from stationary equilibria or with different supersonic converging velocities all arrive at this configuration at the moment of protostar formation.
2. Prior to the point at which cores become supercritical and outside-in collapse begins, the velocities interior to cores are subsonic, even if they are created by highly supersonic flows. In fact, *higher* inflow velocities from ambient gas produce *lower* post-shock velocities within the dense core (see Figures 2–5 and Equation (23)). This result is consistent with observations showing that dense cores are quiescent in their interiors (see, e.g., Myers 1983; Goodman et al. 1998; Lee et al. 2001; Caselli et al. 2002; Kirk et al. 2007; André et al. 2007; Lada et al. 2008).
3. Throughout both the core-building and core-collapse stage, density profiles for cores formed by shocked converging flows can be fitted by BE profiles, but with fitted temperatures  $T_{\text{BE}}$  larger than the true temperature  $T_0$ . The range of temperatures fitted for our models with Mach numbers up to 7 is  $T_{\text{BE}}/T_0 = 1.2\text{--}2.9$ . This result is consistent with observational findings (Kandori et al. 2005; Kirk et al. 2005) that effective temperatures greater than directly measured values (from fitting spectral energy distributions (SEDs)) are usually required in order to fit BE spheres to observed prestellar cores. The largest possible ratio that could be obtained for an isothermal spherical flow is  $T_{\text{BE}}/T_0 = 4.43$ , so that any observed ratio larger than this suggests that magnetic fields contribute appreciable support, or else the core is anisotropic. Dapp & Basu (2009) have also recently pointed out that the temperature fit based on matching a BE profile may be significantly higher than the true kinetic temperature, for clouds in collapsing stages.
4. At the time of collapse, for all Mach numbers the core size and mean density are closely related. We find that  $R_{\text{coll}} \approx 4a(4\pi G\rho_{\text{mean}})^{-1/2}$  within 15% for Mach numbers  $M_a = 1.05\text{--}7$ . This radius is  $\sim 50\%$  larger than the critical radius of a BE sphere with the same mean internal density.
5. As  $M_a$  increases, and assuming a given ambient medium density  $\rho_0$ , the time to reach collapse  $t_{\text{coll}}$  is shorter, the physical size of the core at  $t_{\text{coll}}$  is smaller, the mean internal density at  $t_{\text{coll}}$  is higher, and the mass of the core at  $t_{\text{coll}}$  is lower. For high Mach number, the collapse time and collapse radius are related by  $t_{\text{coll}} \approx 2.6R_{\text{coll}}M_a/a$ . The range of core masses at the time of collapse at different  $M_a$  is consistent with observed core masses, although the specific dependence of core mass on  $M_a$  found in the present work may be sensitive to the spherical converging-flow geometry we have adopted.
6. The durations of the collapse (supercritical) stage and the infall stage of evolution are comparable for all  $M_a$ , and are close to  $t_{\text{ff}}$ . This is consistent with observations indicating

similar lifetimes for prestellar cores and embedded Class 0/I accreting protostars (Beichman et al. 1986; Lee & Myers 1999; Jessop & Ward-Thompson 2000; Kirk et al. 2005; Jørgensen et al. 2007; Hatchell et al. 2007; Enoch et al. 2008; Evans et al. 2009). These stages are preceded by an extended core-building stage, during most of which the core would not be observable because its center-to-edge density contrast is low.

7. The mass accretion rate onto the protostar (or, more realistically, star-disk system if angular momentum were included) peaks at the beginning of the infall stage at a value  $\gg a^3/G$ , and then declines steeply afterward as the material stored in the envelope is exhausted. This result appears to hold regardless of how cores form, as it is consistent with earlier work (see, e.g., Foster & Chevalier 1993; Ogino et al. 1999; Hennebelle et al. 2003; Motoyama & Yoshida 2003; Vorobyov & Basu 2005) for cores initiated from unstable equilibria or which undergo externally induced compression. Later accretion from the ambient medium depends on how long the large-scale cloud maintains a focused converging flow.

As noted above, some of our specific conclusions are likely to change for nonspherical geometry, and for time-dependent rather than steady large-scale inflow. Furthermore, other elements that are present in real star formation have been entirely omitted in these models; these elements include rotation, which would lead to disk formation; protostellar winds, which would sweep up and remove a portion of the envelope during the infall stage, and could prevent late accretion altogether; and magnetic fields, which would alter the timescales and details of the evolutionary stages.

We expect, however, that many of our basic results will carry over even if the idealizations we have adopted are relaxed. While large-scale supersonic converging flows in real GMCs are not generally spherical, the association of observed cores with high-density surroundings suggests that the dense gas in post-shock stagnation regions is still the raw material out of which cores are built. We expect that in general core masses and collapse timescales will decrease with increasing density of the post-shock flow, which itself increases with increasing Mach number. Preliminary simulations of planar converging flows that we have conducted indeed bear out this expectation, showing  $M_{\text{core}} \propto M_a^{-1}$ . For planar converging flows, many cores simultaneously grow and then collapse in the post-shock gas layer; unless this sheet was viewed exactly edge-on, the density jump at the shock front would not be apparent, and cores would be seen as surrounded by moderate-density gas.

We also expect outside-in collapse followed by inside-out infall to be a generic feature of core evolution. Although the duration of this pressure-mediated collapse is  $\sim t_{\text{ff}}$ , it is *unlike* free-fall collapse in a crucial way: the core does not remain nearly uniform. We speculate that the development of stratification during outside-in collapse will suppress growth of perturbations and subfragmentation for the nonspherical case. Even though the increase in density implies that the local Jeans mass becomes smaller and smaller, this is only true in the very center of the core. Instead, we expect that collapse of cores built within shocked converging flows will produce single systems, which may be binary (or multiple) if the angular momentum is sufficient. Nonspherical converging flows that create sheets and filaments of shocked gas and produce many such cores simultaneously could be the progenitors of stellar clusters.

This research was supported by grant NNG-05GG43G from NASA. We are grateful to Phil Myers, Shantanu Basu, and the referee for careful reading and helpful comments on the manuscript.

## REFERENCES

- Alves, J. F., Lada, C. J., & Lada, E. A. 2001, *Nature*, **409**, 159
- André, P., Basu, S., & Inutsuka, S.-i. 2008, *Structure Formation in Astrophysics*, ed. G. Chabrier (Cambridge: Cambridge Univ. Press)
- André, P., Belloche, A., Motte, F., & Peretto, N. 2007, *A&A*, **472**, 519
- Bacmann, A., André, P., Puget, J.-L., Abergel, A., Bontemps, S., & Ward-Thompson, D. 2000, *A&A*, **361**, 555
- Ballesteros-Paredes, J., Klessen, R. S., & Vázquez-Semadeni, E. 2003, *ApJ*, **592**, 188
- Beichman, C. A., Myers, P. C., Emerson, J. P., Harris, S., Mathieu, R., Benson, P. J., & Jennings, R. E. 1986, *ApJ*, **307**, 337
- Bergin, E. A., & Tafalla, M. 2007, *ARA&A*, **45**, 339
- Bodenheimer, P., & Sweigart, A. 1968, *ApJ*, **152**, 515
- Bonnor, W. B. 1956, *MNRAS*, **116**, 351
- Boss, A. P., & Black, D. C. 1982, *ApJ*, **258**, 270
- Broderick, A. E., Keto, E., Lada, C. J., & Narayan, R. 2007, *ApJ*, **671**, 1832
- Caselli, P., Benson, P. J., Myers, P. C., & Tafalla, M. 2002, *ApJ*, **572**, 238
- Dapp, W. B., & Basu, S. 2009, *MNRAS*, **395**, 1092
- Di Francesco, J., Evans, N. J., II, Caselli, P., Myers, P. C., Shirley, Y., Aikawa, Y., & Tafalla, M. 2007, in *Protostars and Planets V*, ed. B. Reipurth, D. Jewitt, & K. Keil (Tucson, AZ: Univ. Arizona Press), 17
- Di Francesco, J., Myers, P. C., Wilner, D. J., Ohashi, N., & Mardones, D. 2001, *ApJ*, **562**, 770
- Ebert, R. 1955, *Z. Astrophys.*, **37**, 217
- Enoch, M. L., Evans, N. J., II, Sargent, A. I., Glenn, J., Rosolowsky, E., & Myers, P. 2008, *ApJ*, **684**, 1240
- Evans, N. J., II, Rawlings, J. M. C., Shirley, Y. L., & Mundy, L. G. 2001, *ApJ*, **557**, 193
- Evans, N. J., II, et al. 2009, *ApJS*, **181**, 321
- Fatuzzo, M., & Adams, F. C. 2002, *ApJ*, **570**, 210
- Foster, P. N., & Chevalier, R. A. 1993, *ApJ*, **416**, 303
- Gómez, G. C., Vázquez-Semadeni, E., Shadmehri, M., & Ballesteros-Paredes, J. 2007, *ApJ*, **669**, 1042
- Goodman, A. A., Barranco, J. A., Wilner, D. J., & Heyer, M. H. 1998, *ApJ*, **504**, 223
- Gregersen, E. M., Evans, N. J., II, Zhou, S., & Choi, M. 1997, *ApJ*, **484**, 256
- Hatchell, J., Fuller, G. A., Richer, J. S., Harries, T. J., & Ladd, E. F. 2007, *A&A*, **468**, 1009
- Heitsch, F., Zweibel, E. G., Slyz, A. D., & Devriendt, J. E. G. 2004, *ApJ*, **603**, 165
- Hennebelle, P., Whitworth, A. P., Gladwin, P. P., & Andre, Ph. 2003, *MNRAS*, **340**, 870
- Hunter, C. 1977, *ApJ*, **218**, 834
- Jessop, N. E., & Ward-Thompson, D. 2000, *MNRAS*, **311**, 63
- Jørgensen, J. K., Johnstone, D., Kirk, H., & Myers, P. C. 2007, *ApJ*, **656**, 293
- Kandori, R., et al. 2005, *AJ*, **130**, 2166
- Keto, E., Broderick, A. E., Lada, C. J., & Narayan, R. 2006, *ApJ*, **652**, 1366
- Kirk, H., Johnstone, D., & Tafalla, M. 2007, *ApJ*, **668**, 1042
- Kirk, J. M., Ward-Thompson, D., & André, P. 2005, *MNRAS*, **360**, 1506
- Kudoh, T., & Basu, S. 2008, *ApJ*, **679**, L97
- Lada, C. J., Muench, A. A., Rathborne, J., Alves, J. F., & Lombardi, M. 2008, *ApJ*, **672**, 410
- Larson, R. B. 1969, *MNRAS*, **145**, 271
- Lee, C. W., & Myers, P. C. 1999, *ApJS*, **123**, 233
- Lee, C. W., Myers, P. C., & Tafalla, M. 1999, *ApJ*, **526**, 788
- Lee, C. W., Myers, P. C., & Tafalla, M. 2001, *ApJS*, **136**, 703
- Li, Z.-Y., & Nakamura, F. 2004, *ApJ*, **609**, L83
- Mac Low, M. M., & Klessen, R. S. 2004, *Rev. Mod. Phys.*, **76**, 125
- Mardones, D., Myers, P. C., Tafalla, M., Wilner, D. J., Bachiller, R., & Garay, G. 1997, *ApJ*, **489**, 719
- McKee, C. F., & Ostriker, E. C. 2007, *ARA&A*, **45**, 565
- Motoyama, K., & Yoshida, T. 2003, *MNRAS*, **344**, 461
- Mouschovias, T. C., & Ciolek, G. E. 1999, in *NATO ASIC Proc. 540: The Origin of Stars and Planetary Systems*, ed. C. J. Lada & N. D. Kylafis (Dordrecht: Kluwer), 305
- Myers, P. C. 1983, *ApJ*, **270**, 105
- Myers, P. C. 2005, *ApJ*, **623**, 280
- Nakamura, F. 1998, *ApJ*, **507**, L165

- Nakamura, F., & Li, Z.-Y. 2008, *ApJ*, **687**, 354
- Ogino, S., Tomisaka, K., & Nakamura, F. 1999, *PASJ*, **51**, 637
- Penston, M. V. 1969, *MNRAS*, **144**, 425
- Peretto, N., André, P., & Belloche, A. 2006, *A&A*, **445**, 979
- Shirley, Y. L., Evans, N. J., II, Rawlings, J. M. C., & Gregersen, E. M. 2000, *ApJS*, **131**, 249
- Shu, F. H. 1977, *ApJ*, **214**, 488
- Shu, F. H., Adams, F. C., & Lizano, S. 1987, *ARA&A*, **25**, 23
- Stone, J. M., & Norman, M. L. 1992, *ApJS*, **80**, 753
- Troland, T. H., & Crutcher, R. M. 2008, *ApJ*, **680**, 457
- Vorobyov, E. I., & Basu, S. 2005, *MNRAS*, **360**, 675
- Walsh, A. J., Bourke, T. L., & Myers, P. C. 2006, *ApJ*, **637**, 860
- Ward-Thompson, D., André, P., Crutcher, R., Johnstone, D., Onishi, T., & Wilson, C. 2007, in *Protostars and Planets V*, ed. B. Reipurth, D. Jewitt, & K. Keil (Tucson, AZ: Univ. Arizona Press), 33
- Ward-Thompson, D., Scott, P. F., Hills, R. E., & Andre, P. 1994, *MNRAS*, **268**, 276
- Whitworth, A., & Summers, D. 1985, *MNRAS*, **214**, 1
- Zhou, S., Evans, N. J., II, Koempe, C., & Walmsley, C. M. 1993, *ApJ*, **404**, 232
- Zweibel, E. G. 2002, *ApJ*, **567**, 962